This is a repository copy of *A systematic review of lumped-parameter equivalent circuit models for real-time estimation of lithium-ion battery states*.

# A Systematic Review of Lumped-Parameter Equivalent Circuit Models for Real-Time Estimation of Lithium-ion Battery States

S. Nejad[a], D. T. Gladwin[a], and D. A. Stone[a]

[a]Department of Electronic and Electrical
Engineering, University of Sheffield,
Sheffield, S1 3JD, United Kingdom

s.nejad@sheffield.ac.uk
d.gladwin@sheffield.ac.uk
d.a.stone@sheffield.ac.uk

**Abstract** – This paper presents a systematic review for the most commonly used lumped-parameter equivalent circuit model structures in lithium-ion battery energy storage applications. These models include the Combined model, Rint model, two hysteresis models, Randles' model, a modified Randles' model and two resistor-capacitor (RC) network models with and without hysteresis included. Two variations of the lithium-ion cell chemistry, namely the lithium-ion iron phosphate (LiFePO$_4$) and lithium nickel-manganese-cobalt oxide (LiNMC) are used for testing purposes. The model parameters and states are recursively estimated using a nonlinear system identification technique based on the dual Extended Kalman Filter (dual-EKF) algorithm. The dynamic performance of the model structures are verified using the results obtained from a self-designed pulsed-current test and an electric vehicle (EV) drive cycle based on the New European Drive Cycle (NEDC) profile over a range of operating temperatures. Analysis on the ten model structures are conducted with respect to state-of-charge (SOC) and state-of-power (SOP) estimation with erroneous initial conditions. Comparatively, both RC model structures provide the best dynamic performance,

29    with an outstanding SOC estimation accuracy. For those cell chemistries with large inherent

30    hysteresis levels (e.g. $LiFePO_4$), the RC model with only one time constant is combined with

31    a dynamic hysteresis model to further enhance the performance of the SOC estimator.

32

33    **Keywords** – battery modelling, persistent excitation, real-time estimation, state-of-charge,

34    state-of-power

35

# 1. Introduction

Due to the growing concerns over the emissions of greenhouse gasses, together with the volatile and ever-increasing cost of fossil fuels, a global shift towards hybrid electric vehicles (HEVs), plug-in hybrid electric vehicles (PHEVs) and battery electric vehicles (BEVs) is apparent. The uptake of these electrified vehicles (EVs) within the transport system not only improves the air quality in dense urban areas, but can also provide a distributed energy storage solution for the implementation of the rapidly evolving smart grid [1]. However, without significant improvements on traction battery technologies and battery management systems (BMSs), the adoption of EVs by consumers is not feasible.

A key function of the BMS is to assess and monitor the performance of the traction battery through accurate characterisation of various battery states. These states include the state-of-charge (SOC – quantity of deliverable ampere-hour charge at any time), state-of-health (SOH – ability of a battery to provide its nominal capacity over its service lifetime), state-of-power (SOP – a quantity describing the battery's power capability) and the state-of-function (SOF – a binary yes/no parameter indicating the battery's ability to complete a task) [2–4].

Whilst direct measurement techniques such as coulomb-counting (integration of battery current over the charge or discharge period) are easy to implement for SOC estimation, they suffer largely from erroneous initialisation of SOC, drifts caused by current sensor noise and battery capacity variations due to temperature and SOH. Moreover, the direct measurement of the other battery states of interest (i.e. SOH, SOP and SOF) for real-time applications is somewhat impossible. Hence, battery models are often utilised within the BMS to indirectly infer and monitor the battery's operation through the measurement of its terminal voltage,

60  current and surface temperature. In addition to accurate characterisation of the battery states,

61  a candidate model is also desired to be computationally efficient. In other words, there should

62  be a balance between model accuracy and complexity so that it can easily be embedded on a

63  simple and inexpensive microprocessor unit (MCU), similar to those found in EV BMS

64  hardware.

65

66  The battery models presented in literature mainly fall into one of the following categories:

67      1. Electrochemical or physics-based models,

68      2. Empirical or data-based models, and

69      3. Equivalent electrical-circuit based models.

70  Electrochemical models (e.g. [5–9]) that aim to capture the dynamic behaviour of battery

71  cells on a macroscopic scale often can achieve high accuracies. These models are defined by

72  a high number of partial differential equations (PDEs) that must be solved simultaneously.

73  The complexity of any electrochemical model is directly related to the number and order of

74  the governing PDEs, which can lead to tremendous requirements for memory and

75  computational power. Another issue that often precludes these models from real-time

76  applications is that due to the large number of unknown variables, they are likely to run into

77  over-fitting problems, increasing the uncertainty in the model's output. Alternatively, these

78  models can be represented by a lower number of 'reduced order' PDEs and by substituting

79  boundary conditions and discretisation, real-time applications may become achievable (e.g.

80  [10–12]). However, this comes at the expense of reduced SOC accuracy and yet the

81  computational burden on the MCU remains questionable.

82

83  Data-based models (e.g. [13–15]) often adopt empirically derived equations from

84  experimental data fittings to infer relationships between various battery parameters such as

85 the terminal voltage, throughput current, surface temperature and SOC. Although these

86 models benefit from simplicity and ease of implementation, they often suffer from

87 inaccuracies of 5-20% mainly due to the highly non-linear behaviour of a battery under a

88 dynamic load profile. In [16,17], the authors took a multiple-model approach to battery

89 modelling using the local model networks (LMN). This technique interpolates between

90 different local linear models to capture the battery's non-linearity due to SOC variations,

91 relaxation, hysteresis, temperature and the battery current effects. One downside of the LMN

92 modelling approach is the excessive requirements for different experiments to train the model

93 in first place. Generally, the data-based model parameters are not physically interpretable,

94 which drops their popularity for in situ estimation and tracking of SOH and SOP.

95 Furthermore, a large cell sample of the same chemistry is required to create a dataset for

96 identification and training of data-based models.

97

98 In [18–20], Plett used a series of models including the combined, simple, zero-state

99 hysteresis, one-state hysteresis and a non-linear enhanced self-correcting (ESC) model to

100 adaptively estimate the battery's SOC. The latter model took into consideration the effects of

101 the current direction, the SOC dependency of open-circuit-voltage (OCV) hysteresis and the

102 relaxation or the charge-recovery effect to improve the model accuracy for dynamic load

103 profiles. In an attempt to model the OCV hysteresis behaviour together with the charge

104 recovery effects, Roscher et al. [21] developed an empirical model whose parameters

105 required off-line identification. In [22], Huria et al. proposed a mathematical model to

106 describe the dynamics of the large hysteresis levels that exist amongst high-power lithium-ion

107 cells. Further on in the paper, this model structure will be referred to as the adaptive

108 hysteresis model.

109

110     The lumped-parameter equivalent circuit models have gained a lot of interest amongst EV

111     designers for real-time battery state estimation and power management purposes. This is due

112     to their simplified mathematical and numerical approaches that minimise the necessity for

113     computationally intensive procedures. Furthermore, there is often a strong physical relation

114     between the constituent model parameters and the underlying electrochemical processes that

115     occur within the battery cells. These models use passive electrical components, such as

116     resistors and capacitors, to mimic the behavioural response of a battery. The simplest

117     equivalent circuit model is in the form of an ideal voltage source in series with a resistor [23].

118     This model assumes that the demand current has no physical influence on the battery, i.e. no

119     core temperature variations or undesired transition effects. More complicated equivalent

120     circuit models include resistor-capacitor (RC) networks to characterise the battery transient

121     responses with different time-constants associated with the diffusion and charge-transfer

122     processes. Depending on the dynamics of the load profile and the required modelling

123     accuracy, the number of the parallel RC branches may vary from one-RC (e.g. [24–27]) to

124     two-RC (e.g. [28–30]). Higher order Models of up to fifth-order have also been used

125     previously in literature (e.g. [31]) to improve the model's impedance response under higher

126     frequencies of operation.

127

128     In literature, there are no studies that compare the accuracy and universality of the reported

129     battery models for real-time estimation of SOC and SOP together. Therefore, this review

130     paper aims to carry out a systematic study of a number of selected lumped-parameter battery

131     models for two variations of the lithium-ion cell chemistry, namely the lithium-ion iron

132     phosphate (LiFePO$_4$) and the lithium nickel-manganese-cobalt oxide (LiNMC). The models

133     of interest in this paper include the combined model, Rint model, One-state hysteresis model

134     by Plett, Huria et al. hysteresis model, one- and two-RC models and one- and two-RC models

135    combined with the hysteresis model proposed by Huria et al [22]. These models were

136    nominated based on the number of their appearances in the literature. The Kalman filter (KF)

137    algorithm is then applied to simultaneously estimate and identify the model parameters in real

138    time. Nevertheless, for those models that are non-linear in parameters (e.g. one- and two-RC

139    models) the extended Kalman filter (EKF) algorithm is adopted.

140

141    This paper is organised as follows. Section 2 describes the experimental configuration for

142    gathering an accurate dataset for both training and verification purposes. Section 3 gives a

143    quantitative definition for the SOC, SOP and SOF. Section 4 provides an overview of the

144    battery model structures of interest in this work. Section 5 describes the real-time system

145    identification technique based on the dual-EKF algorithm for both model parameter

146    identification and battery state estimation. Section 6 compares the voltage prediction and

147    SOC estimation capabilities of the nominated model structures. Furthermore, an optimum

148    model structure will be put forward for real-time SOP and SOF estimation. And finally

149    section 7 concludes this paper.

## 150   2. Battery Dataset Generation

### 151   2.1 Experimental Setup

152    The experimental setup features a multi-channel Maccor battery tester, a built-in-house

153    thermal chamber and a host computer for rig control and data storage. The voltage and

154    current sensors incorporated into each channel of the Maccor system have accuracies of

155    $\pm 0.02\%$ ($0 - 20$ V full-scale) and $\pm 0.05\%$ ($0 - 10$ A full-scale) respectively. Since the current

156    sensor noise is very small and the sampling period is reasonably high ($T_s = 100$ ms), it is safe

157    to assume that the integral of the throughput current over the discharge/charge period

158  represents a "true" measurement of the cell's SOC. Therefore, we use the coulomb-counting

159  technique to systematically compare the accuracy of the model-based SOC estimates.

160

161  The generality of the candidate battery models are demonstrated using two variations of the

162  lithium-ion cell chemistry, (i.e. $LiFePO_4$ and LiNMC). The specifications for the test cells are

163  presented in Table 1. Three cells of each type are used in this work. One reference cell is used

164  for training purposes and the other two cells are used for model verification.

165

166  **Table 1. Specifications for the test cells at 25 °C.**

| Parameter | $LiFePO_4$ | LiNMC |
|---|---|---|
| Rated Capacity | 3300 mAh | 3600 mAh |
| Nominal Voltage | 3.2 V | 3.65 V |
| End-of-Charge Voltage | 3.65 V | 4.2 V |
| End-of-Discharge Voltage | 2.0 V | 2.75 V |
| Nominal Resistance | 30 mΩ | 20 mΩ |

167

168  In order to gather an accurate dataset, a test sequence as presented in Table 2, is designed and

169  implemented. The test sequence starts with incubating the cells in the thermal chamber for 24

170  hours. The chosen dwell time is long enough for the small cylindrical cells to reach a thermal

171  equilibrium prior to any characterisation test. Five temperature settings of 5 °C, 15 °C, 25 °C,

172  35 °C and 45 °C are chosen for comparison of the model performances across various

173  operating conditions. Throughout the tests, the thermal distribution over the cells is assumed

174  constant and the internal temperature variations due to high discharge/charge currents are

175  neglected.

176

177

178 **Table 2. Battery testing procedures.**

| Step | Procedure |
|------|-----------|
| 1. | Set temperature |
| 2. | Capacity test |
| 3. | OCV vs. SOC test |
| 4. | HPPC test |
| 5. | Self-designed pulse test |
| 6. | Multi-cycle NEDC test |

179

## 180  2.2  Capacity Test

181  Initially, each cell undergoes a capacity measurement cycle, which consists of a 0.5 C

182  constant-current discharge until the end-of-discharge voltage has been reached. This is to

183  remove any residual charge left in the cell. After a 60 minute rest period, the cell is re-

184  charged using the standard constant-current constant-voltage (CCCV) scheme at the

185  manufacturer's recommend current and voltage levels. Following a 60 minute rest, the cell

186  under test is discharged at a 0.5 C current level. The quantity of charge removed from the cell

187  is recorded as the maximum discharge capacity at the set temperature, which will be used for

188  SOC calculations.

## 189  2.3  OCV-SOC Relationship

190  In order to generate a function to describe the OCV-SOC relationship, the reference cells

191  were applied with a pulsed-current and relaxation test. The test profile began with a full

192  discharge at a constant current of 0.5 C until the lower voltage thresholds were reached.

193  Then, the cells were re-charged to 100% SOC using the CCCV charging scheme. After a

194  relaxation period of 60 minutes, the first OCV was recorded at SOC = 100%. Furthermore,

195    the cells were discharged in steps of 10% SOC at a current level of 0.5 C for both cell

196    chemistries followed by 60 minute rest periods. This sequence was repeated until the cells

197    were fully discharged. The OCV measurements during the charge half-cycle were also

198    obtained using a similar procedure, where the cells were charged in steps of 10% SOC at a

199    constant current of 0.5 C.

200

201    Upon the completion of the pulsed-current test, the OCV values extracted for both the charge

202    and discharge regimes were used to curve-fit an 8$^{th}$ order polynomial function to describe the

203    average OCV-SOC relationship for both the LiFePO$_4$ and LiNMC cells as,

204

$$V_{OC} = a_8 SOC^8 + \cdots + a_1 SOC + a_0$$

(1)

205

206    The fitted OCV curves at various temperatures are presented in Fig. 1. As can be seen, during

207    the operational SOC range of both battery chemistries (i.e. 20% ≤ SOC ≤ 80%), the OCV-

208    SOC relationship is almost independent of the operating temperature. This finding implies

209    that for practical purposes, one can safely rely on only an OCV curve obtained at a

210    reasonable temperature. However, to keep the modelling uncertainties at a minimum, separate

211    functions are fitted in this work to represent the OCV-SOC relationship at each temperature

212    setting.

213
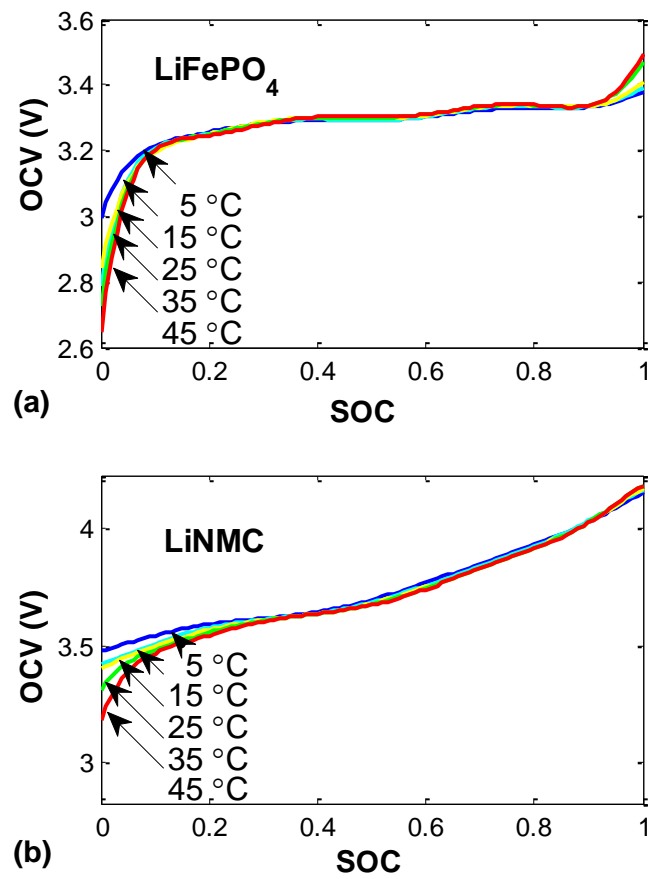
**Fig. 1. The average OCV-SOC relationship for (a) LiFePO₄ and (b) LiNMC reference cells**

215

## 2.4  HPPC Test

217    The Hybrid-Pulse-Power-Characterisation (HPPC) test is a standard procedure developed by

218    the Partnership for New Generation Vehicles (PNGV) [32] used to determine the power and

219    energy capability of a rechargeable battery under both discharge and regenerative charging

220    scenarios. This particular test profile is used in this work to demonstrate the SOP variability

221    as a function of SOC and operating temperature. It should be noted that the profile starts with

222    a preamble discharge and re-charge step as to adjust the cell's SOC to 100% prior to testing.

223    Furthermore the HPPC pulses, as shown in Fig. 2(a), are applied over the SOC range of 10-

224    90% in steps of 10% SOC. A discharge current pulse of 0.5 C is used for both cell

225    chemistries to take the SOC to the next desired level and a 60 minute rest interval is allowed

226    between the HPPC pulse repetitions.

## 227    2.5  Validation Datasets

228    The validation datasets in this work include the results from a self-designed pulsed-current

229    test and a multi-cycle New European Drive Cycle (NEDC) test. The purpose of the self-

230    designed pulsed-current test, as shown in Fig. 2(b), is to dynamically excite the cell under test

231    with variable current amplitudes and durations. Note that the self-designed test profile has a

232    predominant discharge characteristic as to remove charge from the cell under test. The

233    obtained dataset from this test will be used to compare the output accuracy of the model

234    structures under review.

235

236    The multi-cycle NEDC test profile is used to evaluate the adaptability of the battery models

237    for real-time SOC estimation. The test profile starts by removing charge form the cell using a

238    0.5 C current level for both cell chemistries. This step ensures a known initial SOC value of

239    90% is achieved prior to applying the cell under test with 14 consecutive NEDC cycles. A

240    single repetition of the NEDC cycle is illustrated in Fig. 2(c). Upon the completion of every

241    NEDC cycle, a rest period of 15 minutes is allowed before the next cycle commences.

242    Finally, a discharge current pulse of 0.5 C is applied as to fully discharge the cell.

243

244



(a)

245



(b)

246



(c)
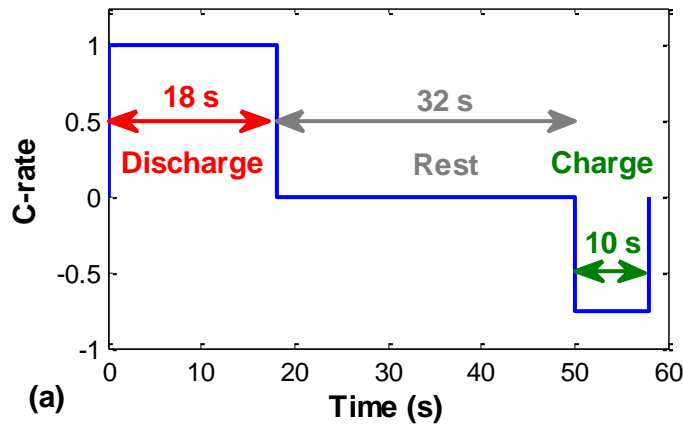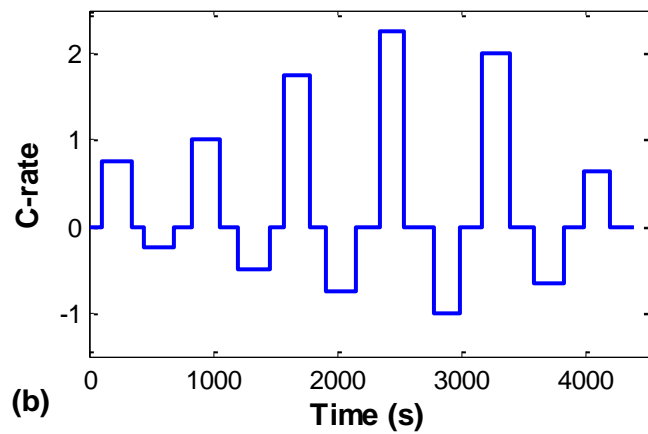
247    **Fig. 2.  Current profiles for a single repetition of the (a) HPPC, (b) self-designed pulsed-current and (c)**

248                                **multi-cycle NEDC test procedures**

249

## 250    3. State Definitions

251    In this paper, SOC is defined as

252

$$SOC(t) = SOC(0) - \frac{\eta_i}{Q_n} \int_0^t i(\tau) \cdot d\tau \tag{2}$$

253

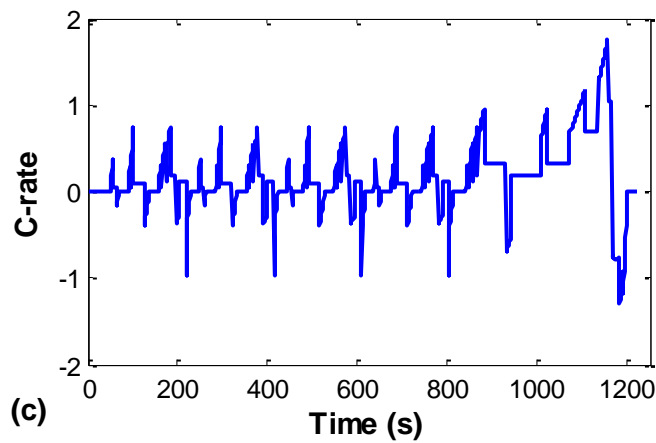254    where $\eta_i$ is the cell's Coulombic efficiency of the cell, $i(t)$ is the instantaneous current and

255    $Q_n = 3600 \times Ah$ is the cell's nominal ampere-hour (Ah) capacity. Conventionally, $\eta_i$ is

256    defined as the ratio of the quantity of charge that is injected into a cell during charging to that

257    removed from the cell during discharging.

258

$$\eta_i = \frac{Q_{\text{discharge}}(\text{Ah})}{Q_{\text{charge}}(\text{Ah})} \times 100\%. \tag{3}$$

259

260    In order to include SOC as an estimable state in the battery models' state-space equations, the

261    coulomb-counter equation given in (2) needs to be converted into discrete form. Thus,

262    assuming a small sampling period (i.e. $T_s = \Delta t \leq 1$ s) and using a rectangular approximation

263    for $SOC(t)$ yields,

264

$$SOC_{k+1} = SOC_k - \left(\frac{\eta_i \cdot T_s}{Q_n}\right) i_k. \tag{4}$$

265

266    Various quantitative definitions for SOP and SOF exist in literature (e.g. [33–35]), which are

267    all associated with the battery's power capabilities. In this paper, we define SOP as the

268    available source or sink power over a short period of $\Delta t$. Using $V_{OC} = f(SOC)$ as defined in

269    (1), the instantaneous discharge or charge power at time step $k$ can be respectively calculated

270    as,

271

$$P_{\text{dis},k} = \frac{V_{\min}(V_{\text{OC},k} - V_{\min})}{\hat{R}_{\text{eq}}} \tag{5}$$

272

$$P_{\text{ch},k} = \frac{V_{\max}(V_{\max} - V_{\text{OC},k})}{\hat{R}_{\text{eq}}} \tag{6}$$

273

274    where $V_{\min}$ and $V_{\max}$ are the minimum and maximum threshold voltages recommended by

275    the manufacturer for a safe operation and $\hat{R}_{\text{eq}}$ is an estimate for the cell's series-equivalent

276    resistance. To this end, we can define SOF in terms of available power as,

277

$$\text{SOF} = \begin{cases} 1, & \text{for } P_{\text{ch},k} \geq P_{\text{req}}^{\text{ch}} \text{ and } P_{\text{dis},k} \geq P_{\text{req}}^{\text{dis}} \\ 0, & \text{for } P_{\text{ch},k} < P_{\text{req}}^{\text{ch}} \text{ and } P_{\text{dis},k} < P_{\text{req}}^{\text{dis}} \end{cases} \tag{7}$$

278

279    where $P_{\text{req}}^{\text{ch}}$ and $P_{\text{req}}^{\text{dis}}$ are the required quantity of charge or discharge power respectively to

280    complete a particular task. Note that the value of $\hat{R}_{\text{eq}}$ in (5) and (6) can be approximated by

281    applying the Thevenin's Theorem to an equivalent circuit model. Alternatively, the voltage

282    and current waveforms obtained for a sequence of HPPC pulses at every SOC value can be

283    used to calculate a value for the cell's discharge or charge resistance as,

284

$$R_{\text{dis}} = \frac{V_0 - V_1}{I_{\text{dis}}}, \qquad R_{\text{ch}} = \frac{V_3 - V_2}{I_{\text{ch}}}. \tag{8}$$

285

286    In (8), $V_0$ and $V_1$ are the cell voltages measured respectively at the start and end of a

287    discharge current pulse, $I_{\text{dis}}$, of duration $\Delta t$ seconds. Similarly, $V_2$ and $V_3$ are the voltage

288    measurements taken for a charge current pulse $I_{\text{ch}}$ of duration $\Delta t$ seconds. The resulting

289    resistances are analogous to the cell's internal resistances and can reflect on the power

290    capability of a cell under operation. Consequently, any variations in the cell's internal

291    resistance as a function of SOC and temperature can affect the quality of the SOP estimate at

292    any time.

293

# 4. Lithium-ion Battery Models

295    The candidate battery model structures for the purpose of this review study are summarised in

296    Table 3. These models form the basis for real-time SOC, SOP and SOF estimation algorithms

297    in most lithium-ion battery energy storage applications.

298

299                             **Table 3. Candidate lithium-ion battery models.**

| Model | Description |
|---|---|
| 1. | Combined model, (9) |
| 2. | Rint model, (10) |
| 3. | Huria et al. Hysteresis model, (11) |
| 4. | Plett Hysteresis model, (14) |
| 5. | Randles' model, (15) |
| 6. | Modified Randles' model, (17) |
| 7. | One-RC model, (18) |
| 8. | Two-RC model, (18) |
| 9. | One-RC model with Hysteresis, (18) + (11) |
| 10. | Two-RC model with Hysteresis, (18) + (11) |

300

## 4.1 The Combined Model

302    The combined model [19] is a very crude approximation of the battery's dynamics. As the

303    name suggests, this model structure is a combination of the Shepherd model [14], Unnewehr

304    and Nasar universal model [36] and the Nernst model [37] given as,

305

$$V_k = \underbrace{K_0 - \frac{K_1}{\mathrm{SOC}_k} - K_2\mathrm{SOC}_k + K_3\ln(\mathrm{SOC}_k) + K_4\ln(1-\mathrm{SOC}_k)}_{V_{\mathrm{OC}} = f(\mathrm{SOC})} - i_k R_\mathrm{s} \tag{9}$$

306

307      where $V_k$ is the battery's terminal voltage and $i_k$ is the throughput current. The battery's

308      internal series resistance is described by $R_\mathrm{s}$ and is a function of temperature and SOC. The

309      constants $K_0$, $K_1$, $K_2$, $K_3$ and $K_4$ are used to describe the battery's OCV dependency on SOC.

310      This model benefits from being linear in parameters and thus simplifies the identification

311      procedure.

## 312    4.2  The Rint Model

313      The internal resistance or Rint model is comprised of an ideal voltage source $V_{\mathrm{OC}}$ to represent

314      the battery's OCV as a function of SOC and a series resistor $R_\mathrm{s}$ that describes the internal

315      ohmic losses [38]. This model structure is also linear in parameters and is very "simple" to

316      implement in real time. However, the model's output equation expressed by (10) is only a

317      crude estimate of the battery's actual terminal voltage, which can result in large uncertainties

318      in SOC and SOP estimates.

319

$$V_k = V_{\mathrm{OC},k} - i_k R_\mathrm{s}. \tag{10}$$

## 320    4.3  The Hysteresis Models

321      The OCV as a function of SOC for the two cell chemistries used in this paper are shown in

322      Fig. 3. It is noted that the OCV obtained after a charge step (see Section 2.3) for both

323  LiFePO$_4$ and LiNMC cells has a higher value than that obtained after a discharge step. In

324  literature, this phenomenon is referred to as hysteresis. In [22], the authors have shown that

325  for high-power LiFePO$_4$ cells, the hysteresis level decreases with increasing rest period

326  allowed immediately after a charge or discharge step. This can be attributed to the

327  thermodynamic origins of the hysteresis effects [39], which requires for a long rest period for

328  the cell to reach an equilibrium potential.

329

330  The hysteresis levels obtained after a one-hour rest period for the two cell chemistries under

331  study are presented in Fig. 3(b) and (d). It is apparent that the hysteresis level for the LiFePO$_4$

332  chemistry is considerably higher than that for the LiNMC chemistry. Moreover, within the

333  useable SOC range of 20% to 80%, the OCV curve for the LiFePO$_4$ chemistry is fairly flat.

334  This implies that for those OCV-based SOC estimators, even a small error in the voltage

335  measurement within this region can result in a large deviation from the actual SOC value.

336  Thus, for a more reliable SOC estimation, a model structure of the cell's hysteresis behaviour

337  is of necessity.

338

339  To overcome the effect of hysteresis, different modelling approaches have been reported in

340  literature (e.g. [40]). For those battery chemistries that pose a relatively small hysteresis level

341  (e.g. LiNMC), often a direct approach is adopted [19]. This technique can be achieved either

342  by evaluating the arithmetic mean or minimising the global squared-error between the charge

343  and discharge OCV points obtained separately at the same SOC. However, for those

344  chemistries with larger hysteresis levels (e.g. LiFePO$_4$), the direct methods would lead to

345  large uncertainties in the SOC estimate. Therefore, more comprehensive models are required.

346

347      **(a)**                                  **(b)**

348      **(c)**                                  **(d)**
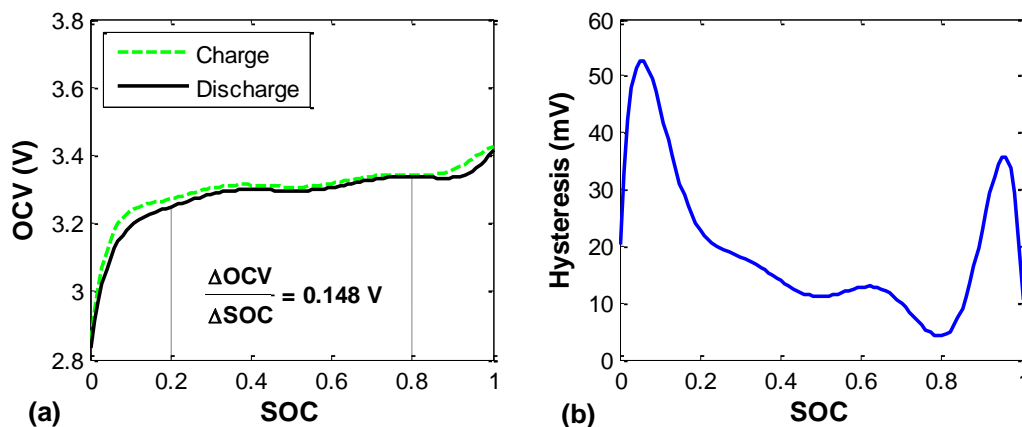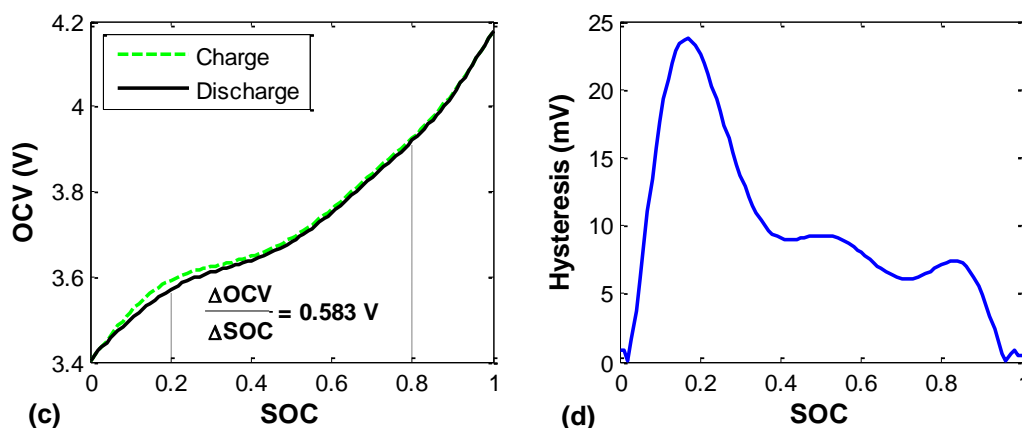
349      **Fig. 3. Open circuit voltage and hysteresis level for LiFePO$_4$ and LiNMC cell chemistries at 25 °C**

350

351 In [21], the authors develop an empirically-derived hysteresis model for LiFePO$_4$ cells

352 comprising of two parts; first part captures the dynamics of the OCV hysteresis as a function

353 of SOC and an identifiable hysteresis factor that determines the position of the OCV curve

354 with respect to the charge and discharge OCV curves, and the second part considers the SOC-

355 dependent recovery effects (i.e. the time taken for the cell to reach a final equilibrium

356 potential after a current interruption at a given SOC). This results in a comprehensive

357 representation of the cell's OCV during operation. However, due to the empirical nature of

358 the model structure, a training dataset is required to identify the model parameters off-line.

359

360    For the purpose of this study, we put the focus on the hysteresis models presented in [19] and

361    [22] whose parameters can possibly be identified recursively in real time, without the

362    necessity for various training datasets. Another example of on-line OCV hysteresis treatment

363    can be found in [41]. The first hysteresis model is developed based on an algorithm presented

364    by Huria et al. [22] and is defined as,

365

$$\nabla V_{OC} = \frac{dV_{OC}}{dSOC} = \begin{cases} \dfrac{dV_{OC,ch}}{dSOC} + m(V_{OC,ch} - V_{OC}), & \text{for } \dfrac{dSOC}{dt} \geq 0 \\ \dfrac{dV_{OC,dis}}{dSOC} + m(V_{OC,dis} - V_{OC}), & \text{for } \dfrac{dSOC}{dt} < 0 \end{cases}. \tag{11}$$

366

367    which determines the gradient of $V_{OC} = f(SOC)$ as a function of the rate-of-change of SOC

368    and its distance away from the major hysteresis loop formed by the charge, $V_{OC,ch}$, and

369    discharge, $V_{OC,dis}$, OCV curves. The dimensionless coefficient $m$ determines how fast $V_{OC}$

370    transitions towards $V_{OC,ch}$ or $V_{OC,dis}$ after a preceding charge or discharge current pulse

371    respectively. In order to compare the performance of the two hysteresis models discussed in

372    this section, algorithm (11) is combined with the Rint model (10) to give,

373

$$V_k = (V_{OC,k} + \nabla V_{OC,k}) - i_k R_s \tag{12}$$

374

375    where $\nabla V_{OC,k}$ is the $V_{OC}$ derivative attained at time step $k$.

376

377    In [19] Plett developed a model to describe the hysteresis effects using a differential equation

378    in both time and SOC such as,

379

$$\frac{dh(SOC,t)}{dSOC} = \gamma \text{sgn}(\dot{SOC})\left(H(SOC,\dot{SOC}) - h(SOC,t)\right) \tag{13}$$

380

381 where $h(\text{SOC}, t)$ is a function to describe the hysteresis voltage, $H(\text{SOC}, \dot{\text{SOC}})$ defines the

382 maximum positive and negative hysteresis as a function of SOC and rate-of-change of SOC,

383 $\gamma$ is a tuneable factor to control the rate-of-decay of hysteresis towards the major loop and

384 $\dot{\text{SOC}} = d\text{SOC}/dt$ is the rate-of-change of SOC. Now, using the definitions given in (1) and

385 (2) and rearranging (13) as a differential equation in time only, the cell model's state-space

386 equations become,

387

$$h_{k+1} = \exp\left(-\left|\frac{\eta_i i_k \gamma T_s}{Q_n}\right|\right) h_k + \left(1 - \exp\left(-\left|\frac{\eta_i i_k \gamma T_s}{Q_n}\right|\right)\right) H(\text{SOC}, \dot{\text{SOC}})$$

$$V_k = V_{\text{OC},k} - i_k R_s + h_k.$$

(14)

388

389 ## 4.4 The Randles' Model

390 The Randles' model was originally developed for lead-acid batteries [42–44]. However, in

391 recent years their utilisation in lithium-ion battery modelling has been sighted [45]. Fig. 4(a)

392 shows the Randles' equivalent circuit diagram for a typical lithium-ion cell, where $R_s$ is the

393 series resistance, $R_d$ models the cell's no-load self-discharge (typically $\sim 70\text{k}\,\Omega$ ), $C_b$

394 represents the bulk charge storage of the cell, $C_s$ represents the electrodes' double-layer effect

395 and $R_t$ is the charge-transfer resistance. The voltage $V_{Cb}$ across $C_b$ is analogous to the cell's

396 OCV and the model's output response can be expressed as,

397

$$\begin{bmatrix} V_{Cb_{k+1}} \\ V_{Cs_{k+1}} \end{bmatrix} = \begin{bmatrix} e^{\frac{-T_s}{R_d C_b}} & 0 \\ 0 & e^{\frac{-T_s}{R_t C_s}} \end{bmatrix} \begin{bmatrix} V_{Cb_k} \\ V_{Cs_k} \end{bmatrix} + \begin{bmatrix} R_d\left(1 - e^{\frac{-T_s}{R_d C_b}}\right) & 0 \\ 0 & R_t\left(1 - e^{\frac{-T_s}{R_t C_s}}\right) \end{bmatrix} i_k$$

(15)

$$V_k = V_{Cb,k} - V_{Cs,k} - i_k R_s.$$

398

399      Gould et al. [28] developed a new battery model through the star-delta transformation of the

400      original Randles' circuit. This particular model, as shown in Fig. 4(b), consists of the same

401      number of parameters as the Randles' model with a slight modification in the way the

402      transient states are represented. In [28], it is shown that when applied with real-time state

403      observers such as the Utkin and Kalman Filter, the parallel reconfiguration of the Randles'

404      model states can yield a better SOC estimate. Thus, the adaptability of this model structure

405      for online SOC and SOP estimation will be evaluated in this study. Consequently, Mapping

406      the Randles' model parameters as per [28] and solving for the output equation in discrete

407      form yields,

408

$$C_{\mathrm{n}} = C_{\mathrm{b}}^2/(C_{\mathrm{b}} + C_{\mathrm{s}}), \qquad C_{\mathrm{p}} = C_{\mathrm{p}}C_{\mathrm{s}}/(C_{\mathrm{b}} + C_{\mathrm{s}}),$$

$$R_{\mathrm{n}} = R_{\mathrm{t}}(C_{\mathrm{b}} + C_{\mathrm{s}})^2/C_{\mathrm{b}}^2, \qquad R_{\mathrm{p}} = R_{\mathrm{d}} + R_{\mathrm{t}} \tag{16}$$

409

$$\begin{bmatrix} V_{\mathrm{Cp}_{k+1}} \\ V_{\mathrm{Cn}_{k+1}} \end{bmatrix} = \begin{bmatrix} e^{\frac{-T_{\mathrm{s}}}{\tau_{\mathrm{p}}}} & \dfrac{R_{\mathrm{T}}}{R_{\mathrm{n}}}\left(1 - e^{\frac{-T_{\mathrm{s}}}{\tau_{\mathrm{p}}}}\right) \\ \left(1 - e^{\frac{-T_{\mathrm{s}}}{\tau_{\mathrm{n}}}}\right) & e^{\frac{-T_{\mathrm{s}}}{\tau_{\mathrm{n}}}} \end{bmatrix} \begin{bmatrix} V_{\mathrm{Cp}_k} \\ V_{\mathrm{Cn}_k} \end{bmatrix} + \begin{bmatrix} R_{\mathrm{T}}\left(e^{\frac{-T_{\mathrm{s}}}{\tau_{\mathrm{p}}}} - 1\right) & 0 \\ 0 & 0 \end{bmatrix} i_k \tag{17}$$

$$V_k = V_{\mathrm{Cp},k} - i_k R_{\mathrm{s}}$$

410

411      where $R_{\mathrm{T}} = R_{\mathrm{p}}R_{\mathrm{n}}/(R_{\mathrm{p}} + R_{\mathrm{n}})$, $\tau_{\mathrm{n}} = R_{\mathrm{n}}C_{\mathrm{n}}$ and $\tau_{\mathrm{p}} = R_{\mathrm{T}}C_{\mathrm{p}}$.

412 ## 4.5 The RC Model

413      The resistor-capacitor (RC) or the Thevenin equivalent circuit model is a modification of the

414      Rint model, as shown in Fig. 4(c). This model is comprised of an ideal voltage source to

415      represent the cell's OCV at partial equilibrium as a function of SOC, a series ohmic

416 resistance $R_s$ and $n$ number of series-connected RC branches. Depending on the dynamics of

417 the intended application, the number of the RC branches may vary. For most power

418 applications, one RC branch is adequate (e.g. [46–48]) to describe the long time-constant

419 reactions associated with the diffusion of active species into the electrolyte.

420

421 Considering applications with faster transients, the short time-constant reactions associated

422 with the charge-transfer and the double-layer effect of the electrodes can be modelled with

423 additional RC branches (e.g. [49–52]). However, there is a trade-off between accuracy and

424 complexity, which must be considered for a particular application. In this paper, the

425 performance of one-RC and two-RC models are reviewed analytically. Without loss of

426 generality, the electrical behaviour of an nth order RC model in its discrete form can be
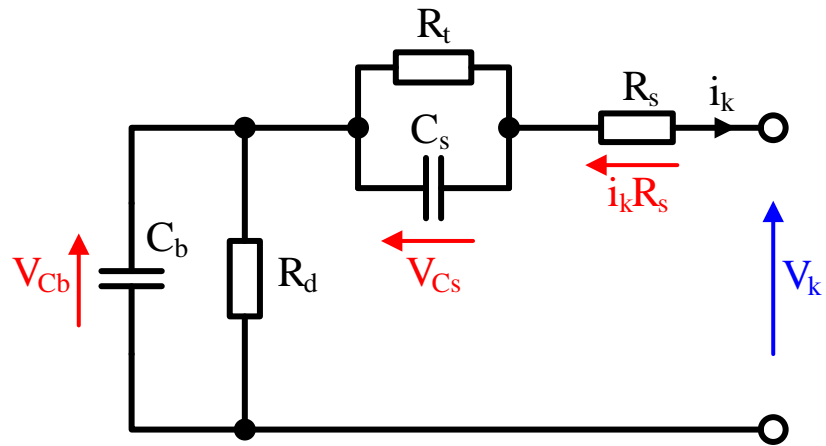
427 expressed as,

428

$$\begin{bmatrix} V_{RC1_{k+1}} \\ \vdots \\ V_{RCn_{k+1}} \end{bmatrix} = \begin{bmatrix} e^{\frac{-T_s}{R_1 C_1}} & \cdots & 0 \\ \vdots & \ddots & \vdots \\ 0 & \cdots & e^{\frac{-T_s}{R_n C_n}} \end{bmatrix} \begin{bmatrix} V_{RC1_k} \\ \vdots \\ V_{RCn_k} \end{bmatrix} + \begin{bmatrix} R_1 \left(1 - e^{\frac{-T_s}{R_1 C_1}}\right) & \cdots & 0 \\ \vdots & \ddots & \vdots \\ 0 & \cdots & R_n \left(1 - e^{\frac{-T_s}{R_n C_n}}\right) \end{bmatrix} i_k \quad (18)$$

$$V_k = V_{OC}(SOC_k) - i_k R_s - V_{RC1} - \cdots - V_{RCn}.$$

429

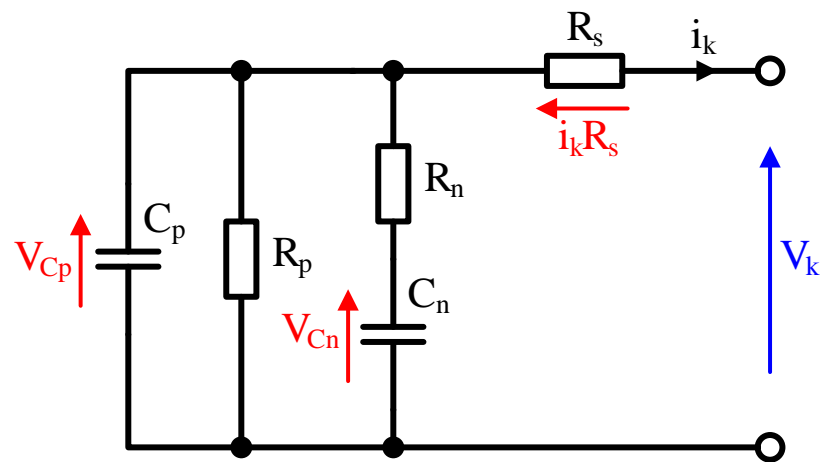430

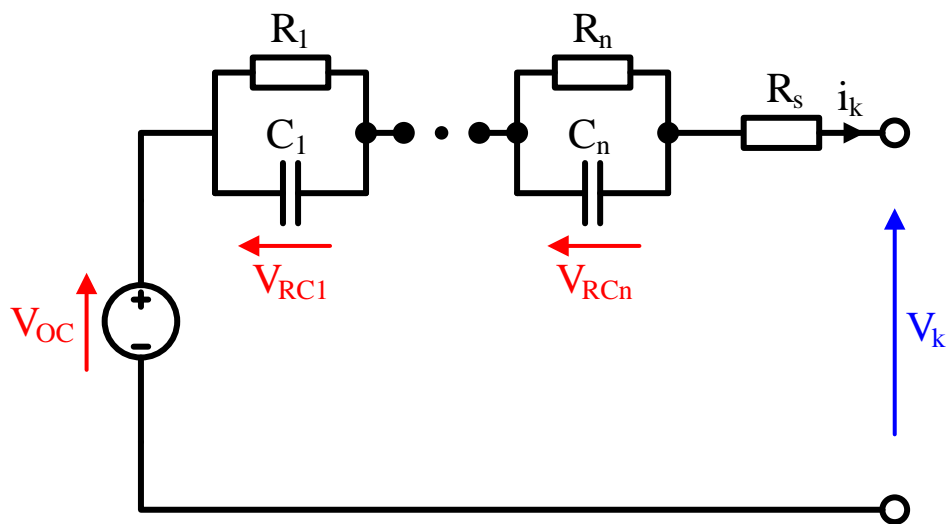431       **(a)**



432       **(b)**



433       **(c)**

434       **Fig. 4. The equivalent ci4rcuit diagrams for (a) Randles', (b) modified Randles' and (c) n-RC model**

435                            **structures**

## 436   5. Online Non-linear System Identification

437   The Kalman filter is a recursive set of equations that allow for state estimation and parameter

438   identification of linear time-invariant systems [53]. On the other hand, the EKF is an ad hoc

439   solution for the identification of non-linear time-varying systems such that, the non-linear

440   model describing the underlying dynamics of the system is linearised about the filter's

441   current estimated trajectory. For simultaneous estimation of both model states and

442   parameters, two separate are often incorporated in a parallel configuration. This method is

443   referred to in literature as the dual-EKF algorithm [54–57].

444

445   Essentially, the dual-EKF combines the state and weight filters, where the model states,

446   including SOC, are estimated by the state filter and the model parameters are identified

447   recursively by the weight filter. Due to its robustness, the Kalman filter algorithm is often

448   utilised in the battery energy and/or power management systems to overcome a wide range of

449   problems (e.g. [58–61]). Therefore, this popular system identification technique is applied to

450   the candidate battery model structures given in Table 3.

## 451   5.1   Dual-EKF System Identification

452   With the assumption that the cell terminal current $i_k$ and voltage $V_k$ are the only measurable

453   quantities, the EKF state filter can be designed such that,

454

$$x_{k+1} = f(x_k, u_k, \theta_k) + w_k$$

$$y_k = h(x_k, u_k, \theta_k) + v_k$$

$$w_k \sim N(0, Q_x)$$  \hfill (19)

$$v_k \sim N(0, R_x)$$

455

456    where $x_k \in \mathbb{R}^n$ is a vector containing the model states to be predicted in a minimum variance

457    sense, $\theta_k \in \mathbb{R}^q$ contains the time-varying model parameters, $u_k \in \mathbb{R}^p$ is the exogenous

458    model input, $y_k \in \mathbb{R}^m$ is the output and $w_k \in \mathbb{R}^n$ and $v_k \in \mathbb{R}^m$ are the zero-mean process

459    and measurement noises of covariance $Q_k^x$ and $R_k^x$ respectively. The non-linear function $f(\cdot,\cdot,\cdot$

460    $)$ relates the states estimated at discrete time $k-1$ to the states at the current time step $k$ and

461    $h(\cdot,\cdot,\cdot)$ maps the updated states to the measurements at time step $k$. Assuming that the

462    parameters vary slowly over time, the weight EKF can be designed to adaptively provide an

463    estimate $\hat{\theta}$ of the true model parameters. Thus, the state-space model for the weight filter is

464    given as,

465

$$\theta_{k+1} = \theta_k + r_k$$

$$d_k = h(x_k, u_k, \theta_k) + e_k$$

$$r_k \sim N(0, Q_\theta) \tag{20}$$

$$e_k \sim N(0, R_\theta)$$

466

467    where the "dynamics" of changes in $\hat{\theta}_k$ are attributed to a small "imaginary" white noise $r_k \in$

468    $\mathbb{R}^p$ of covariance $Q_k^\theta$ that evolves the parameters over time. The output equation $d_k \in \mathbb{R}^m$ is

469    given as a measurable function of $\hat{\theta}_k$ and a white noise $e_k \in \mathbb{R}^m$ of covariance $R_k^\theta$ to account

470    for the sensor noise and modelling uncertainties.

471

472    Due to the time-variability of the model parameters, it is imperative that the cell data

473    collected using the current profiles presented in section 2 convey continual information on

474    the parameters to be estimated. This condition is referred to in the system identification

475    literature as the "persistence of excitation" (PE) [62]. In many real-time battery state

476    estimation problems, the load-current profile may not fully satisfy the PE criterion. For those

477    observer-based SOC estimators such as the extended Luenberger observer, sliding mode or

478    adaptive observers, if the PE condition is not sufficiently satisfied, the gains tend to approach

479    infinity and divergence occurs [62]. Nevertheless, the EKF algorithm seems to operate well

480    under such conditions without any divergence (e.g. [63–66]). This is due to the presence of

481    the persistently exciting process and measurement noise, which are assumed to be white

482    colour for the dual-EKF estimator presented here. Note that white noise has a continuous

483    spectrum over the whole frequency range and thus is persistently exciting for any finite order

484    [67,68].

485

486    For brevity, a summary of the dual-EKF algorithm is presented in Table 4. Note that the

487    algorithm is initialised by assuming a priori knowledge of the model states and parameters

488    are available. However, in practice the initial system information are unknown. Thus, the

489    states and the parameters are set to their best guess values at $k = 0$ so that $\hat{\theta}_0^+ = E[\theta_0]$ and

490    $\hat{x}_0^+ = E[x_0]$ . The estimation error covariance matrices are also initialised as $P_{\theta,0}^+ =$

491    $E\left[\left(\theta - \hat{\theta}_0^+\right)\left(\theta - \hat{\theta}_0^+\right)^T\right]$ and $P_{x,0}^+ = E[(x - \hat{x}_0^+)(x - \hat{x}_0^+)^T]$.

492

493    Each time step, the algorithm first updates the state and parameter estimates $\hat{x}_k^-$ and $\hat{\theta}_k^-$ and

494    their error covariance $P_{\tilde{x},k}^-$ and $P_{\tilde{\theta},k}^-$ respectively, by propagating them forward in time. Note

495    that for the parameter time-update equation (25), the new parameter estimate $\hat{\theta}_k^-$ is equal to

496    the previous estimate $\hat{\theta}_{k-1}^+$ with an increase in its uncertainty due to the presence of the white

497    process noise $r_k$. After a measurement has been taken at time step $k$, both filters take this

498    measurement into consideration to update the state and parameter estimates $\hat{x}_k^+$ and $\hat{\theta}_k^+$ their

499    corresponding uncertainties as $P_{\tilde{x},k}^+$ and $P_{\tilde{\theta},k}^+$ respectively. In (26) and (27), the measurement-

500     update error covariance matrices $P_{\tilde{x},k}^+$ and $P_{\tilde{\theta},k}^+$ are given in their Joseph forms to ensure a

501     numerically robust algorithm.

502

503     It is noted that for the weight filter's measurement-update equations given in (27), the total-

504     differential $H_k^\theta$ of the model output equation $h(\cdot,\cdot,\cdot)$ with respect to parameters $\theta$ is required.

505     Therefore, by decomposing the total-derivative into partial-derivatives, $H_k^\theta$ is computed

506     recursively as the following set of equations,

507

$$
\left.
\begin{aligned}
H_k^\theta &= \left.\frac{\mathrm{d}h(\hat{x}_k^-, u_k, \theta)}{\mathrm{d}\theta}\right|_{\theta=\hat{\theta}_k^-} \\[2mm]
\frac{\mathrm{d}h(\hat{x}_k^-, u_k, \theta)}{\mathrm{d}\theta} &= \frac{\partial h(\hat{x}_k^-, u_k, \theta)}{\partial\theta} + \frac{\partial h(\hat{x}_k^-, u_k, \theta)}{\partial\hat{x}_k^-}\cdot\frac{\mathrm{d}\hat{x}_k^-}{\mathrm{d}\theta} \\[2mm]
\frac{\mathrm{d}\hat{x}_k^-}{\mathrm{d}\theta} &= \frac{\partial f(\hat{x}_{k-1}^+, u_{k-1}, \theta)}{\partial\theta} + \frac{\partial f(\hat{x}_{k-1}^+, u_{k-1}, \theta)}{\partial\hat{x}_{k-1}^+}\cdot\frac{\mathrm{d}\hat{x}_{k-1}^+}{\mathrm{d}\theta} \\[2mm]
\frac{\mathrm{d}\hat{x}_{k-1}^+}{\mathrm{d}\theta} &= \frac{\mathrm{d}\hat{x}_{k-1}^-}{\mathrm{d}\theta} - L_{k-1}^x\frac{\mathrm{d}h(\hat{x}_{k-1}^-, u_{k-1}, \theta)}{\mathrm{d}\theta}.
\end{aligned}
\right\}
\tag{21}
$$

508

509     Since $L_{k-1}^x$ is weakly related to the parameter estimates $\theta$, it can be safely neglected in (21) to

510     improve the efficiency of the weight filter. Furthermore, $\mathrm{d}\hat{x}_{k-1}^+/\mathrm{d}\theta$ is set to zero at $k = 0$

511     and the three total-derivatives are updated recursively. In order to ensure the divergence of

512     the state and weight filers, it is important to tune the error covariance matrices. In our case,

513     the tuning variables are the measurement and process noise covariance matrices $R_x$ and $Q_x$

514     for the state and $R_\theta$ and $Q_\theta$ for the weight filters respectively. These parameters are initialised

515     at time step $k = 0$ as,

$$
\begin{aligned}
Q_x &= \mathrm{diag}_p\{1\times10^{-6}\}, & P_{x,0}^+ &= \mathrm{diag}_p\{10\}, & R_x &= 10 \\[2mm]
Q_\theta &= \mathrm{diag}_q\{1\times10^{-8}\}, & P_{\theta,0}^+ &= \mathrm{diag}_q\{10\}, & R_\theta &= 10
\end{aligned}
\tag{22}
$$

516

517    where diag{·} is a diagonal matrix of size $p$ for the state and $q$ for the weight EKFs

518    respectively.

519 **Table 4. Summary of the Dual-EKF algorithm for battery model state and parameter estimation.**

**Initialisation:**

$$\hat{\theta}_0^+ = E[\theta_0], \qquad P_{\theta,0}^+ = E\left[(\theta - \hat{\theta}_0^+)(\theta - \hat{\theta}_0^+)^T\right]$$
$$\hat{x}_0^+ = E[x_0], \qquad P_{x,0}^+ = E[(x - \hat{x}_0^+)(x - \hat{x}_0^+)^T]$$

(23)

**Time-update equations for state filter:**

$$\hat{x}_k^- = f\left(\hat{x}_{k-1}^+, u_{k-1}, \hat{\theta}_k^-\right)$$
$$P_{\tilde{x},k}^- = F_{k-1} P_{\tilde{x},k-1}^+ F_{k-1}^T + Q_x$$

(24)

**Time-update equations for weight filter:**

$$\hat{\theta}_k^- = \hat{\theta}_{k-1}^+$$
$$P_{\tilde{\theta},k}^- = P_{\tilde{\theta},k-1}^+ + Q_\theta$$

(25)

**Measurement-update equations for state filter:**

$$L_k^x = P_{\tilde{x},k}^- (H_k^x)^T \left[H_k^x P_{\tilde{x},k}^- (H_k^x)^T + R_x\right]^{-1}$$
$$\hat{x}_k^+ = \hat{x}_k^- + L_k^x\left[y_k - h\left(\hat{x}_k^-, u_k, \hat{\theta}_k^-\right)\right]$$
$$P_{\tilde{x},k}^+ = (I - L_k^x H_k^x) P_{\tilde{x},k}^- (I - L_k^x H_k^x)^T + L_k^x R_x (L_k^x)^T$$

(26)

**Measurement-update equations for weight filter:**

$$L_k^\theta = P_{\tilde{\theta},k}^- \left(H_k^\theta\right)^T \left[H_k^\theta P_{\tilde{\theta},k}^- \left(H_k^\theta\right)^T + R_\theta\right]^{-1}$$
$$\hat{\theta}_k^+ = \hat{\theta}_k^- + L_k^\theta\left[d_k - h\left(\hat{x}_k^-, u_k, \hat{\theta}_k^-\right)\right]$$
$$P_{\tilde{\theta},k}^+ = \left(I - L_k^\theta H_k^\theta\right) P_{\tilde{\theta},k}^- \left(I - L_k^\theta H_k^\theta\right)^T + L_k^\theta R_\theta \left(L_k^\theta\right)^T$$

(27)

where

$$F_{k-1} = \left.\frac{\partial f\left(x_{k-1}, u_{k-1}, \hat{\theta}_k^-\right)}{\partial x_{k-1}}\right|_{x_{k-1}=\hat{x}_{k-1}^+}, \qquad H_k^x = \left.\frac{\partial h\left(x_k, u_k, \hat{\theta}_k^-\right)}{\partial x_k}\right|_{x_k=\hat{x}_k^-},$$
$$H_k^\theta = \left.\frac{dh(\hat{x}_k^-, u_k, \theta)}{d\theta}\right|_{\theta=\hat{\theta}_k^-}.$$

(28)

520

521 # 6. Results and Discussion

522 A statistical analysis of the test results was performed. Fig. 5 presents the average root-mean-

523 squared-error (RMSE) voltage for each set of LiFePO$_4$ and LiNMC cells for the self-designed

524 pulse test results. In order to mitigate the SOC dependency of the OCV functions, the true

525 SOC values obtained using the coulomb-counting technique were used to compute the RMSE

526 values for each model structure. It is evident that the Rint model has the largest error for both

527 lithium-ion cell chemistries. This is due to the absence of any transient states as to capture the

528 underlying dynamics of the electrochemical and thermodynamic processes.

529

530 The hysteresis models perform consistently better compared to the simple Rint model. This

531 improvement is attributed to the fact that there exists a hysteresis level for both LiFePO$_4$ and

532 LiNMC cell chemistries, which needs considering for more accurate cell modelling.

533 Although similar results are achieved by the two hysteresis models (3 and 4), the model

534 structure proposed by Huria et al. [22] is comparatively more favourable in real-time

535 applications as it only has one identifiable parameter. This further reduces the computational

536 burden on the BMS. The Randles' and the modified Randles' models both have two

537 capacitors to include the OCV and the transients associated with the diffusion effects

538 respectively. However, a large error is induced due to the instabilities in the battery model

539 states.

540

541 Compared to other structures, the one- and two-RC models both demonstrate excellent

542 modelling capabilities. These two models have a separate empirical function as to describe

543 the cell's OCV as a function of SOC. It is observable that by including the OCV hysteresis as

544 one of the EKF states, an even better modelling result in terms of RMSE is achievable.

545    **(a)**



546    **(b)**
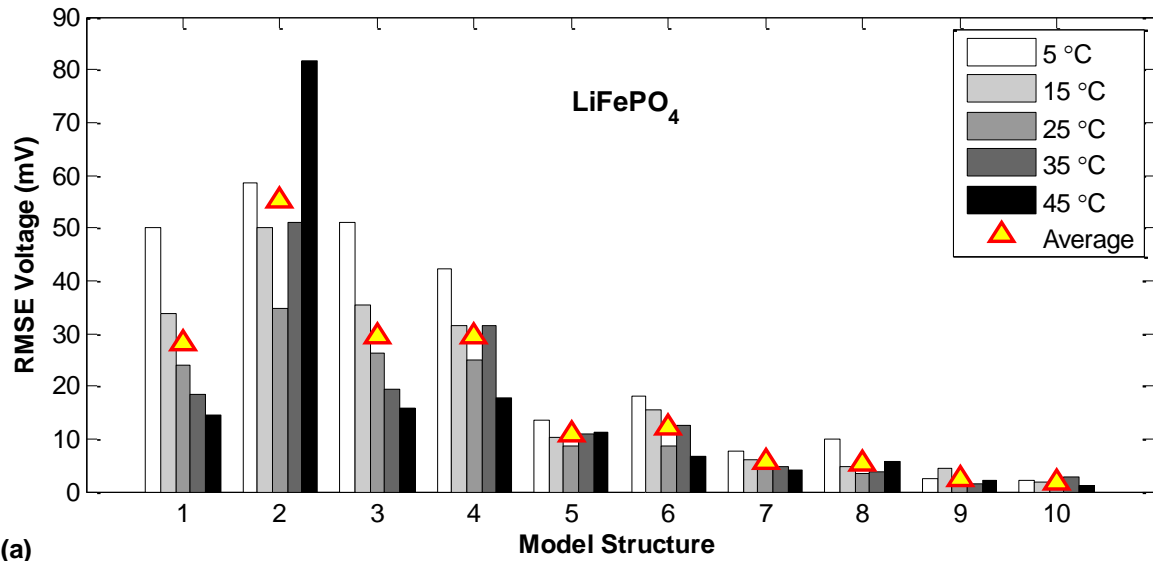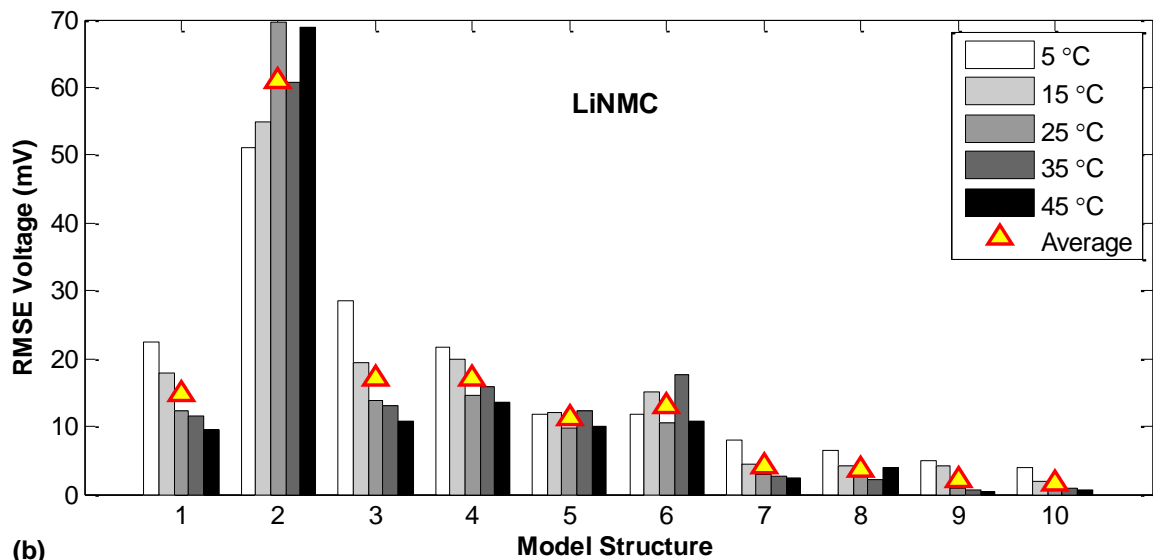
547    **Fig. 5. Average modelling error for the self-designed pulse test for (a) LiFePO₄ and (b) LiNMC set of cells**

548    **over the temperature range 5-45 °C**

549

550    In order to study the SOC estimation and tracking capability of each model structure, the

551    results for the multi-cycle NEDC test over the SOC range of 5-90% were used. The dual-EKF

552    algorithm was initialised with the best-guess values for the model parameters and the SOC

553    state was set to its true value. Fig. 6 presents the estimated cell voltage for one NEDC cycle

554    at SOC = 64% for one of the LiFePO₄ test cells. The results obtained for the LiNMC cells

555  pose a similar behaviour. It can be noted that the two-RC model structure with hysteresis

556  included has the closest fit to the true cell voltage.

557

558  (a)  (b)



559  (c)  (d)
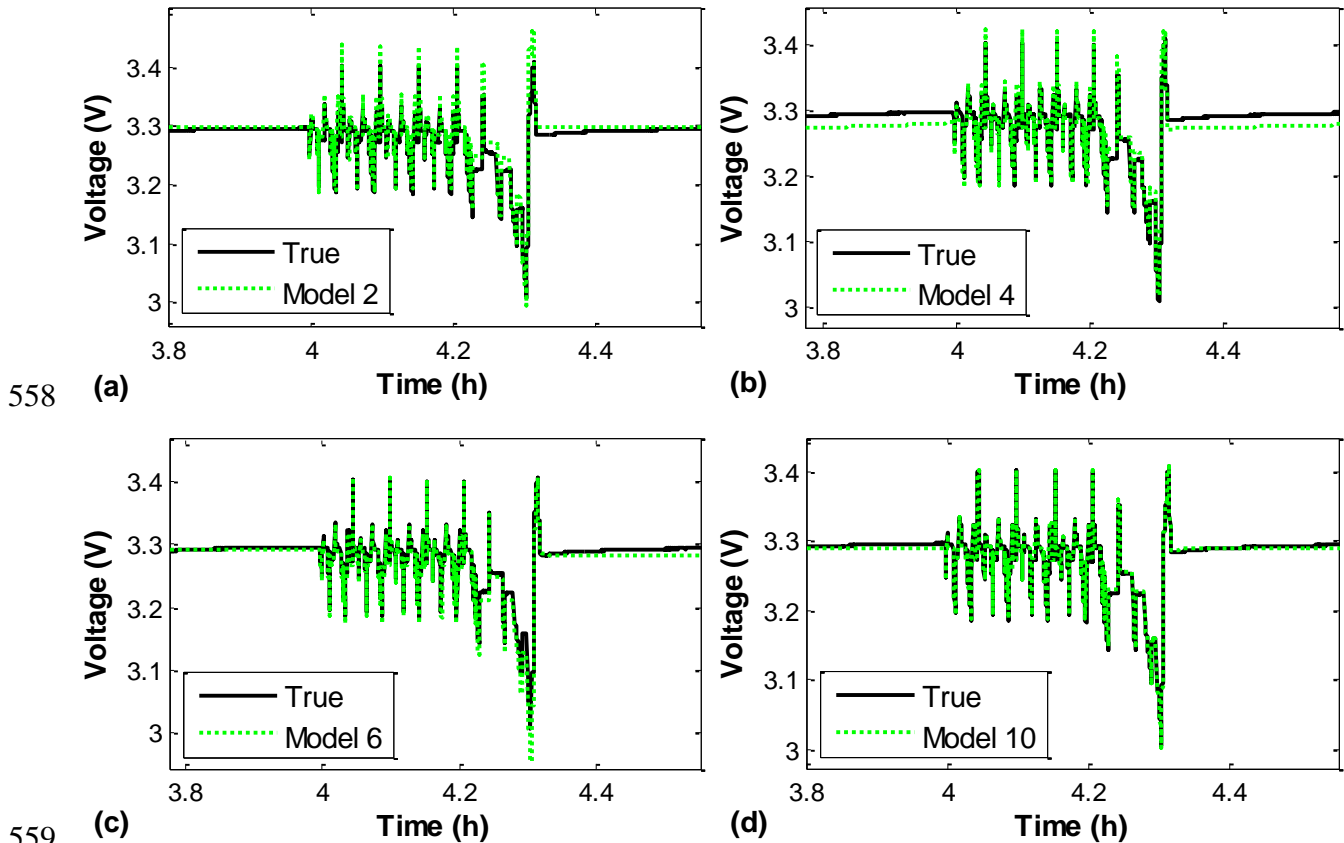
560  **Fig. 6. Estimated voltage from one NEDC cycle for (a) the Rint, (b) the One-state Hysteresis, (c) the**

561  **modified Randles' and (d) the Two-RC model with hysteresis for a LiFePO₄ cell at 25 °C**

562

563  Fig. 7 illustrates the resulting model-based SOC estimation errors at five different

564  temperature settings. The average SOC errors for the three LiFePO₄ set of cells are shown in

565  Fig. 7(a) and those for the LiNMC set of cells are shown in Fig. 7(b). The EKF SOC state for

566  all models was correctly initialised to 90% and the filter and hysteresis states were set to zero.

567  It can be noted that at low operating temperatures, the induced SOC error is the largest. This

568  is due to the fact that at low temperatures, the inherent electrochemical reactions are

569    significantly slower. Thus, it becomes more difficult to model the underlying cell dynamics,

570    leading to a larger modelling and SOC error.

571

572    **(a)**



573    **(b)**
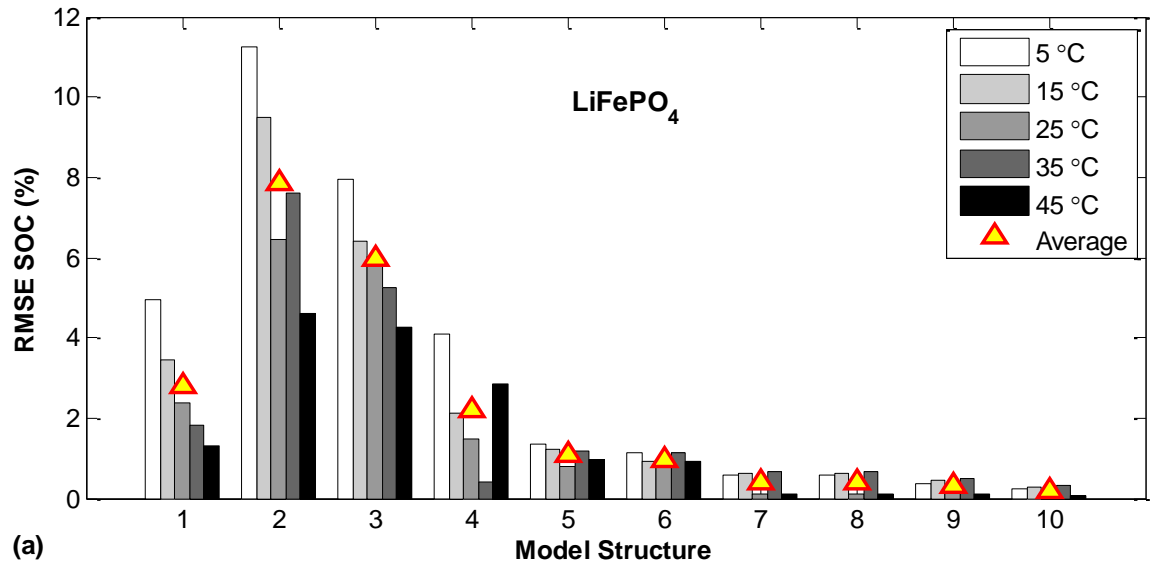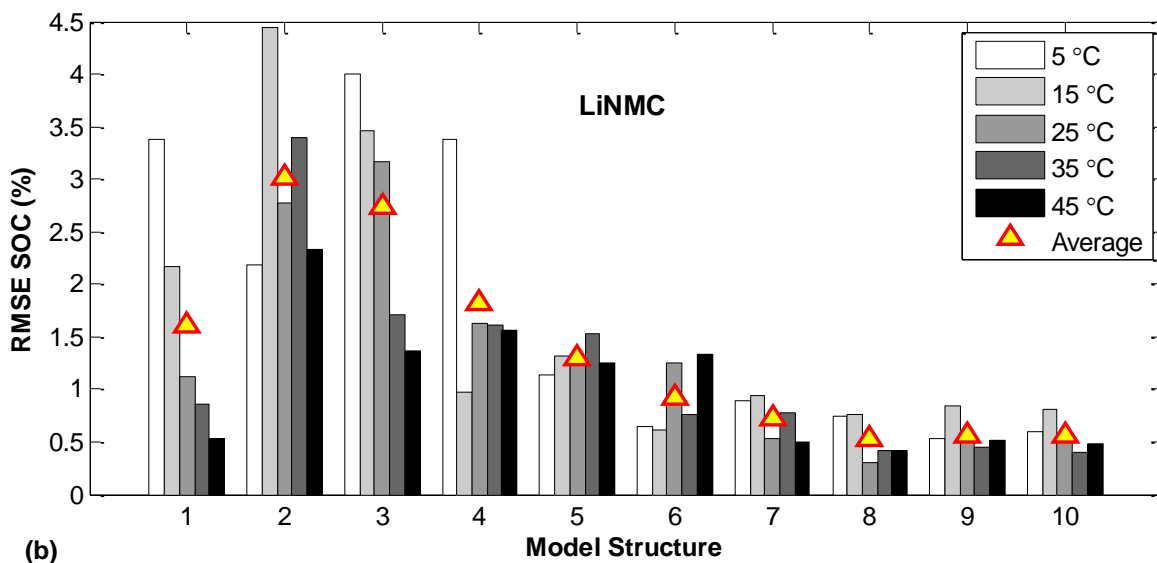
574    **Fig. 7. Average SOC estimation error for the multi-cycle NEDC test for (a) LiFePO₄ and (b) LiNMC set**

575    **of cells over the temperature range 5-45 °C**

576

577    The average SOC errors in Fig. 7 show that, the one- and two-RC model structures pose a

578    considerably better performance for SOC estimation in real time for both cell chemistries.

579    This can be attributed to the enhanced characterisation of the charge-transfer and diffusion

34

580    effects by the model states. Moreover, by including the hysteresis effects in the RC-network

581    model structures, a further improvement in the SOC estimate can be achieved.

582

583    Thus far, the SOC estimation results presented have been obtained using correct initialisation

584    for the EKF's SOC state. In practice, the EKF would be initialised with a "best" estimate for

585    SOC, which is usually realised based on OCV measurements prior to a load connection

586    and/or using the cell's most recent history of usage. Either way results in an inaccurate a

587    priori estimate for the SOC state, which can be exacerbated if the measured OCV lies within

588    the flat region of operation for the $LiFePO_4$ chemistry or the cell has not rested long enough.

589    Therefore, we may now extend our investigation by comparing the estimation results

590    attainable using incorrect EKF initialisation for the ten model structures.

591

592    Using the measurements recorded for the pulsed-current test profile (see Fig. 2(b)) at 25 °C,

593    SOC was estimated for all the $LiFePO_4$ and LiNMC test cells under three different EKF

594    initialisation scenarios. Firstly, the SOC state was correctly initialised to 100% and the results

595    are presented in Table 5. As can be seen, all the model structures are able to achieve a SOC

596    estimate that is within the standard ±5% error bound, given correct initialisation of the SOC

597    state. Secondly, the SOC state was incorrectly initialised to 80% instead of 100%. The results

598    are presented in Table 6. It is evident that compared to other model structures, both RC

599    models with and without the hysteresis included achieved outstanding SOC estimation errors.

600    Finally, the SOC state was incorrectly set to 60% instead of 100%. Similar results are

601    obtainable as presented in Table 7. It should be noted that the SOC error statistics for the

602    three SOC initialisation cases given here were computed by excluding the first hour of the

603    SOC data. This allowed for a reasonable convergence towards the "actual" SOC for all the

604    model structures.

605  **Table 5. SOC estimation results for the pulsed-current test profile at 25 °C with correct initialisation of**

606  **100%.**

| Model | LiFePO₄ | | | LiNMC | | |
|---|---|---|---|---|---|---|
| | Average Error (%) | Maximum Error (%) | Standard deviation of error | Average Error (%) | Maximum Error (%) | Standard deviation of error |
| **1.** | 3.93 | 5.27 | 1.53e-4 | 5.24 | 6.80 | 1.46e-3 |
| **2.** | 2.13 | 9.63 | 1.94e-3 | 3.09 | 11.11 | 6.08e-3 |
| **3.** | 3.17 | 14.35 | 1.10e-3 | 2.80 | 9.78 | 7.77e-3 |
| **4.** | 2.73 | 8.93 | 3.22e-3 | 4.95 | 14.76 | 1.46e-2 |
| **5.** | 3.88 | 5.86 | 2.61e-3 | 6.47 | 16.32 | 3.78e-3 |
| **6.** | 3.03 | 6.02 | 7.21e-4 | 2.20 | 5.21 | 8.43e-3 |
| **7.** | 2.66 | 10.74 | 1.05e-3 | 2.15 | 7.98 | 5.95e-3 |
| **8.** | 2.65 | 10.64 | 1.06e-3 | 2.15 | 7.78 | 5.99e-3 |
| **9.** | 1.39 | 8.58 | 6.56e-4 | 2.89 | 9.69 | 6.55e-3 |
| **10.** | 1.44 | 6.78 | 1.35e-3 | 2.15 | 7.96 | 5.99e-3 |

607

608

609  **Table 6. SOC estimation results for the pulsed-current test profile at 25 °C with incorrect initialisation of**

610  **80% when actual SOC = 100%.**

| Model | LiFePO₄ | | | LiNMC | | |
|---|---|---|---|---|---|---|
| | Average Error (%) | Maximum Error (%) | Standard deviation of error | Average Error (%) | Maximum Error (%) | Standard deviation of error |
| **1.** | 13.19 | 14.82 | 5.6e-4 | 5.23 | 7.17 | 2.06e-3 |
| **2.** | 6.33 | 11.39 | 6.5e-3 | 3.09 | 10.91 | 4.2e-3 |
| **3.** | 3.40 | 14.65 | 1.6e-3 | 2.80 | 9.79 | 6.2e-3 |
| **4.** | 6.96 | 13.67 | 1.1e-2 | 4.95 | 16.16 | 1.0e-2 |
| **5.** | 3.62 | 6.47 | 3.5e-3 | 6.47 | 15.72 | 3.41e-3 |
| **6.** | 5.07 | 9.46 | 2.9e-4 | 2.20 | 6.79 | 2.70e-3 |
| **7.** | 3.03 | 11.18 | 8.5e-4 | 2.15 | 8.03 | 5.16e-3 |
| **8.** | 3.02 | 11.06 | 9.0e-4 | 2.14 | 8.01 | 5.16e-3 |
| **9.** | 2.28 | 11.03 | 6.8e-4 | 2.89 | 9.69 | 7.05e-3 |
| **10.** | 2.01 | 8.37 | 1.4e-3 | 2.15 | 8.01 | 5.11e-3 |

611

612     **Table 7. SOC estimation results for the pulsed-current test profile at 25 °C with incorrect initialisation of**

613     **60% when actual SOC = 100%.**

| Model | LiFePO₄ | | | LiNMC | | |
|---|---|---|---|---|---|---|
| | Average Error (%) | Maximum Error (%) | Standard deviation of error | Average Error (%) | Maximum Error (%) | Standard deviation of error |
| **1.** | 13.45 | 14.82 | 4.57e-3 | 10.00 | 10.78 | 1.05e-3 |
| **2.** | 19.58 | 35.74 | 6.24e-4 | 3.54 | 10.94 | 2.97e-3 |
| **3.** | 3.72 | 14.70 | 2.35e-3 | 3.27 | 9.80 | 5.28e-3 |
| **4.** | 16.20 | 31.63 | 2.86e-3 | 6.56 | 16.52 | 1.03e-2 |
| **5.** | 8.61 | 16.98 | 2.87e-3 | 6.60 | 15.98 | 3.15e-3 |
| **6.** | 11.42 | 21.17 | 4.93e-4 | 2.55 | 5.97 | 1.95e-3 |
| **7.** | 3.12 | 11.25 | 8.50e-4 | 2.33 | 8.07 | 4.55e-3 |
| **8.** | 3.12 | 11.12 | 8.50e-4 | 2.32 | 8.05 | 4.50e-3 |
| **9.** | 2.47 | 11.17 | 3.21e-4 | 2.78 | 9.69 | 7.35e-3 |
| **10.** | 2.34 | 8.80 | 5.69e-4 | 2.34 | 8.06 | 4.40e-3 |

614

615     As presented in Table 6 and Table 7, the best SOC estimation results with incorrectly

616     initialised filter states are realised with the hysteresis model 3 and the one- and two-RC

617     models 7 and 8 respectively. It is apparent that containing the transient effects in a cell model

618     not only improves the characterisation of a cell under load conditions in real time (see Fig. 5),

619     but also results in a more robust SOC estimator. Furthermore, to reduce the uncertainties in

620     the SOC estimate, the hysteresis functions can possibly be merged with the RC models

621     resulting in a better SOC convergence.

622

623     Using the HPPC method [32], the cell discharge resistance and power for every LiFePO₄ and

624     LiNMC test cell under a current pulse with duration of 18 seconds, over a SOC range of 10-

625     90% at five different operating temperatures is calculated. The averaged-results for the two

626     sets of chemistries are presented in Fig. 8. Whereas Fig. 8(a) and (b) demonstrate the

627     variation of the discharge cell resistance calculated using (8), Fig. 8(c) and (d) display how

628    the quantity of available discharge power for a fixed current pulse duration may vary with

629    respect to SOC and temperature for the LiFePO$_4$ and LiNMC cells respectively. It can be

630    noted that at high temperature and SOC values, the cell resistance is smallest for both

631    chemistries, resulting in a larger quantity of power being available for discharge. Moreover,

632    at high SOC values, the corresponding OCV is also larger, which further improves the cell's

633    capability to source power, without violating the safe operating voltage thresholds.

634

635    As defined by (5) and (6), the quality of the estimated instantaneous discharge or charge

636    power largely depends on the accuracy of the identified cell resistance under various

637    operating scenarios. Using the EKF-identified model parameters obtained for each test cell

638    under a single HPPC repetition at 25 °C and SOC = 90%, the Thevenin equivalent circuit

639    resistance, $R_{eq}$, for every model structure presented in this paper is calculated. The obtained

640    model-based cell resistances for each set of chemistries are then averaged and compared to

641    the average of the charge and discharge resistances given by (8) for the same HPPC profile.

642    The results are presented in Table 8. It is evident that the two-RC model and the one-RC with

643    adaptive hysteresis model provide the best estimates for the cell's equivalent resistance,

644    which can be used to improve the quality of the model-based SOP estimate.

645

646
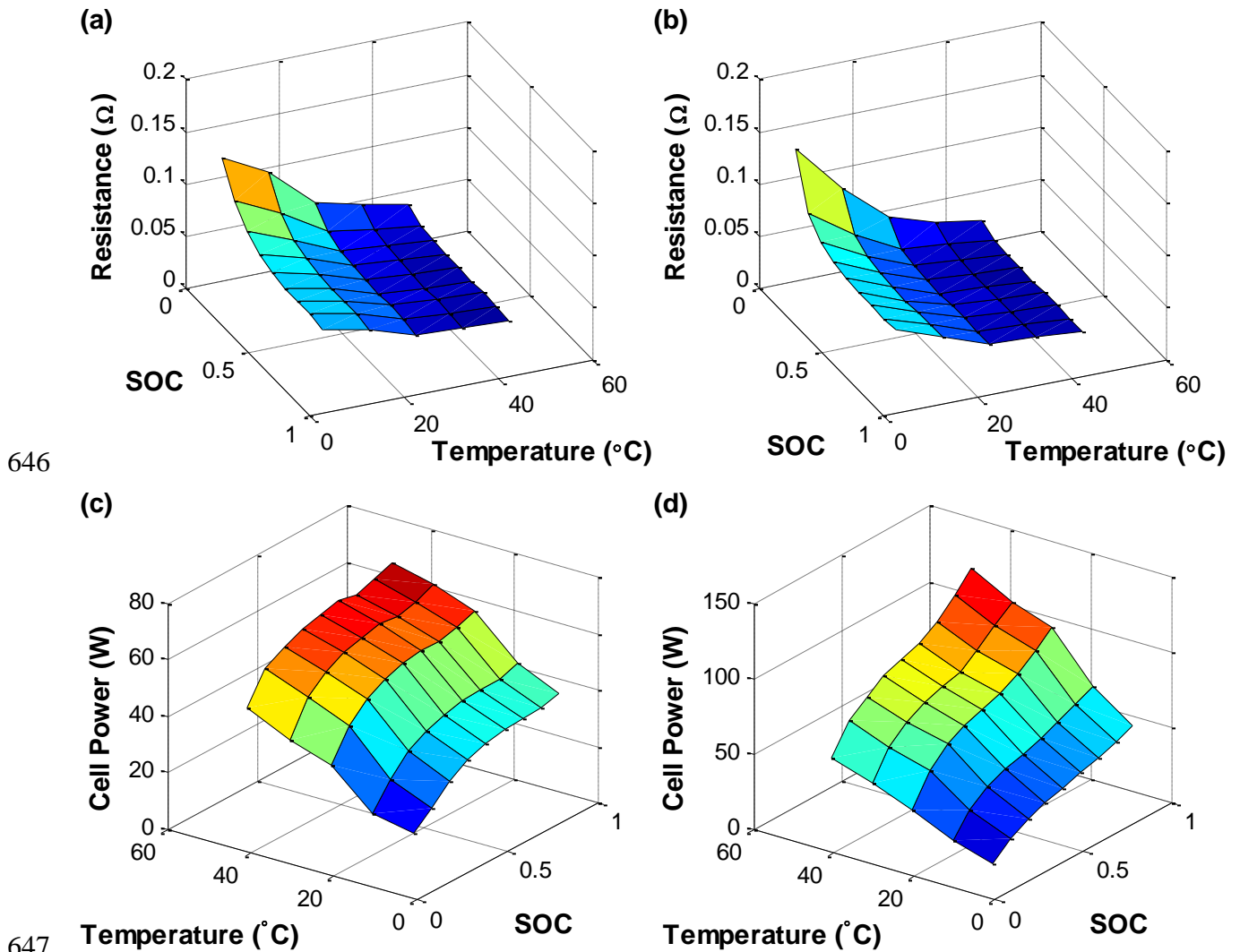
647

**Fig. 8. Comparison of (a) and (b) internal series resistances and (c) and (d) calculated discharge power**

**using the HPPC method for the LiFePO$_4$ and LiNMC cells as a function of SOC and temperature**

648

649

650

651 Note that for a reliable SOP assessment, an accurate SOC estimate is also required, which in

652 turn reflects on the accuracy of the cell's predicted OCV in (5) and (6). Thus, to this end, the

653 two-RC model structure can be nominated as an optimum selection with only two estimable

654 states and five identifiable parameters for superior cell dynamic modelling and joint SOC and

655 SOP estimation results. Alternatively, for cell chemistries with large inherent hysteresis

656 levels, the one-RC with hysteresis model is preferred.

657

658    **Table 8. Comparison of the EKF identified equivalent cell resistance with that calculated for the LiFePO₄**

659    **and LiNMC cells for a single HPPC repetition at 25 °C and SOC = 90%.**

| Model | LiFePO₄ | | LiNMC | |
|-------|---------|---|-------|---|
|       | EKF Identified $R_{\text{eq}}$ (mΩ) | Mean Error (mΩ) | EKF Identified $R_{\text{eq}}$ (mΩ) | Mean Error (mΩ) |
| **1.** | 35.5 | 8.1 | 26.5 | 7.8 |
| **2.** | 38.4 | 5.2 | 28.3 | 6.0 |
| **3.** | 45.6 | 2.0 | 46.4 | 12.1 |
| **4.** | 38.4 | 5.2 | 28.3 | 6.0 |
| **5.** | 37.9 | 5.7 | 29.4 | 4.9 |
| **6.** | 36.4 | 7.2 | 27.8 | 6.5 |
| **7.** | 48.2 | 4.6 | 29.5 | 4.8 |
| **8.** | 47.0 | 3.4 | 30.2 | 4.1 |
| **9.** | 46.0 | 2.4 | 32.7 | 1.6 |
| **10.** | 47.3 | 3.7 | 36.6 | 2.3 |

660

# 7. Conclusion

662    This paper has systematically reviewed the most common lumped-parameter equivalent

663    circuit models used in lithium-ion battery energy storage applications based on their number

664    of appearances in literature. The merits for comparison were modelling accuracy in terms of

665    average root-mean-squared-error for two sets of lithium-ion cells of different electrode

666    chemistries, namely the LiFePO₄ and LiNMC. The generality of each model structure was

667    examined over a temperature range of 5-45 °C. The battery models' parameters and states

668    were recursively estimated using a nonlinear system identification technique based on the

669    dual-EKF algorithm. Furthermore, the dynamic performance of each model structure for joint

670    estimation of SOC and SOP were discussed. The results suggested that the two-RC model

671    structure, with two estimable states and five identifiable parameters, is an optimum choice for

672    implementation of most battery energy and power management strategies. Alternatively, for

673 cell chemistries with large inherent hysteresis levels, the one-RC model with hysteresis

674 included is preferred without an increase in complexity.

675

676 ## Acknowledgment

679

# References

[1]   H. Rahimi-Eichi, U. Ojha, F. Baronti, M. Chow, Ind. Electron. Mag. IEEE 7 (2013) 4–16.

[2]   T. Kim, Y. Wang, H. Fang, Z. Sahinoglu, T. Wada, S. Hara, W. Qiao, J. Power Sources 295 (2015) 16–27.

[3]   W. Waag, C. Fleischer, D.U. Sauer, J. Power Sources 258 (2014) 321–339.

[4]   L. Lu, X. Han, J. Li, J. Hua, M. Ouyang, J. Power Sources 226 (2013) 272–288.

[5]   S. Jung, J. Power Sources 264 (2014) 184–194.

[6]   A. Khandelwal, K.S. Hariharan, V.S. Kumar, P. Gambhire, S.M. Kolake, D. Oh, S. Doo, J. Power Sources 248 (2014) 101–114.

[7]   N.A. Chaturvedi, R. Klein, (2010) 1997–2002.

[8]   K. Smith, Control Syst. IEEE (2010) 18–25.

[9]   J. Marcicki, A.T. Conlisk, G. Rizzoni, J. Power Sources 251 (2014) 157–169.

[10]  G.K. Prasad, C.D. Rahn, J. Dyn. Syst. Meas. Control 136 (2014) 041012.

[11]  J.L. Lee, L.L. Aldrich, K.D. Stetzel, G.L. Plett, J. Power Sources 255 (2014) 85–100.

[12]  C. Speltino, D. Di Domenico, G. Fiengo, a. Stefanopoulou, Proc. 48h IEEE Conf. Decis. Control Held Jointly with 2009 28th Chinese Control Conf. (2009) 3276–3281.

[13]  C.M. Shepherd, J. Electrochem. Soc. 112 (1965) 657–664.

[14]  S. Li, B. Ke, in:, IEEE Power Energy Soc. Gen. Meet., 2011, pp. 1–8.

[15]  O. Tremblay, M. Ieee, L. Dessaint, S.M. Ieee, A. Dekkiche, (2007) 284–289.

[16]  J. Unger, C. Hametner, S. Jakubek, M. Quasthoff, J. Power Sources 269 (2014) 883–897.

[17]  C. Hametner, S. Jakubek, J. Power Sources 238 (2013) 413–421.

[18]  G.L. Plett, J. Power Sources 134 (2004) 252–261.

[19]  G.L. Plett, J. Power Sources 134 (2004) 262–276.

[20]  G.L. Plett, J. Power Sources 134 (2004) 277–292.

[21]  M.A. Roscher, D.U. Sauer, J. Power Sources 196 (2011) 331–336.

707    [22]    T. Huria, G. Ludovici, G. Lutzemberger, J. Power Sources 249 (2014) 92–102.

708    [23]    H. He, R. Xiong, J. Fan, Energies 4 (2011) 582–598.

709    [24]    H. Rahimi-Eichi, F. Baronti, M.-Y. Chow, in:, Ind. Electron. (ISIE), 2012 IEEE Int.
710           Symp., 2012, pp. 1336–1341.

711    [25]    Y.-H. Chiang, W.-Y. Sean, J.-C. Ke, J. Power Sources 196 (2011) 3921–3932.

712    [26]    A.H. Ranjbar, A. Banaei, A. Khoobroo, B. Fahimi, Smart Grid, IEEE Trans. 3 (2012)
713           360–367.

714    [27]    J. Kim, B. Cho, Veh. Technol. IEEE Trans. 60 (2011) 4249–4260.

715    [28]    C.R. Gould, C.M. Bingham, D.A. Stone, P. Bentley, IEEE Trans. Veh. Technol. 58
716           (2009) 3905–3916.

717    [29]    T. Kim, W. Qiao, Energy Conversion, IEEE Trans. 26 (2011) 1172–1180.

718    [30]    M. Sitterly, L.Y. Wang, G.G. Yin, C. Wang, Sustain. Energy, IEEE Trans. 2 (2011)
719           300–308.

720    [31]    D. Andre, M. Meiler, K. Steiner, H. Walz, T. Soczka-Guth, D.U. Sauer, J. Power
721           Sources 196 (2011) 5349–5356.

722    [32]    U.S. Department of Energy, PNGV Battery Test Manual, 2001.

723    [33]    S. Wang, M. Verbrugge, J.S. Wang, P. Liu, J. Power Sources 196 (2011) 8735–8741.

724    [34]    G. Plett, Veh. Technol. IEEE Trans. 53 (2004) 1586–1593.

725    [35]    L.W. Juang, P.J. Kollmeyer, T.M. Jahns, R.D. Lorenz, 2012 IEEE Energy Convers.
726           Congr. Expo. (2012) 1819–1826.

727    [36]    L.E. Unnewehr, S.A. Nasar, in:, John Wiley & Sons, Inc., New York, 1982, pp. 81–91.

728    [37]    D. Linden, T.B. Reddy, Linden's Handbook of Batteries, Fourth, McGraw-Hill
729           Education, New York, 2010.

730    [38]    V.H. Johnson, J. Power Sources 110 (2002) 321–329.

731    [39]    M.S. R. Khatib, A.L. Dalverny, M.L.D. M. Gaberscek, J. Phys. Chem. 117 (2013)
732           837–849.

733    [40]    A.A.-H. Hussein, N. Kutkut, I. Batarseh, 2011 Twenty-Sixth Annu. IEEE Appl. Power
734           Electron. Conf. Expo. (2011) 1790–1794.

735    [41]    S. Schwunk, N. Armbruster, S. Straub, J. Kehl, M. Vetter, J. Power Sources 239
736           (2013) 705–710.

737    [42]   A.J. Fairweather, M.P. Foster, D.A. Stone, J. Power Sources 207 (2012) 56–59.

738    [43]   M. Shahriari, M. Farrokhi, IEEE Trans. Ind. Electron. 60 (2013) 191–202.

739    [44]   B.S. Bhangu, P. Bentley, D.A. Stone, C.M. Bingham, in:, Veh. Power Propulsion,
740            2005 IEEE Conf., 2005, p. 10 pp.–.

741    [45]   C. Gould, J. Wang, D. Stone, M. Foster, Int. Symp. Power Electron. Power Electron.
742            Electr. Drives, Autom. Motion (2012) 353–358.

743    [46]   H. Rahimi-eichi, S. Member, M. Chow, (2012).

744    [47]   F. Sun, R. Xiong, H. He, J. Power Sources 259 (2014) 166–176.

745    [48]   M.A. Roscher, O.S. Bohlen, D.U. Sauer, Energy Conversion, IEEE Trans. 26 (2011)
746            737–743.

747    [49]   S. Nejad, D.T. Gladwin, D.A. Stone, in:, Ind. Electron. Soc. IECON 2014 - 40th Annu.
748            Conf. IEEE, 2014, pp. 5660–5665.

749    [50]   J. Remmlinger, M. Buchholz, M. Meiler, P. Bernreuter, K. Dietmayer, J. Power
750            Sources 196 (2011) 5357–5363.

751    [51]   M. Ouyang, G. Liu, L. Lu, J. Li, X. Han, J. Power Sources 270 (2014) 221–237.

752    [52]   C.Y. Chun, J. Baek, G.-S. Seo, B.H. Cho, J. Kim, I.K. Chang, S. Lee, J. Power Sources
753            273 (2015) 255–263.

754    [53]   R.E. Kalman, Trans. ASME-Journal Basic Eng. 82 (1960) 35–45.

755    [54]   I. Kim, IEEE Trans. Power Electron. 25 (2010) 1013–1022.

756    [55]   J. Kim, S. Lee, B.H. Cho, Power Electron. IEEE Trans. 27 (2012) 436–451.

757    [56]   D. Andre, C. Appel, T. Soczka-Guth, D.U. Sauer, J. Power Sources 224 (2013) 20–27.

758    [57]   R. Xiong, X. Gong, C.C. Mi, F. Sun, J. Power Sources 243 (2013) 805–816.

759    [58]   Y. He, X. Liu, C. Zhang, Z. Chen, Appl. Energy 101 (2013) 808–814.

760    [59]   L. Zhong, C. Zhang, Y. He, Z. Chen, Appl. Energy 113 (2014) 558–564.

761    [60]   J. Remmlinger, M. Buchholz, T. Soczka-Guth, K. Dietmayer, J. Power Sources (2012)
762            1–7.

763    [61]   J. Du, Z. Liu, Y. Wang, Control Eng. Pract. 26 (2014) 11–19.

764    [62]   F. Auger, M. Hilairet, J.M. Guerrero, E. Monmasson, T. Orlowska-Kowalska, S.
765            Katsura, Ind. Electron. IEEE Trans. 60 (2013) 5458–5471.

766   [63]   H. He, R. Xiong, X. Zhang, F. Sun, J. Fan, Veh. Technol. IEEE Trans. 60 (2011)
767          1461–1469.

768   [64]   C. Hu, B.D. Youn, J. Chung, Appl. Energy 92 (2012) 694–704.

769   [65]   D. Andre, a. Nuhic, T. Soczka-Guth, D.U. Sauer, Eng. Appl. Artif. Intell. 26 (2013)
770          951–961.

771   [66]   B. Pattipati, C. Sankavaram, K.R. Pattipati, Syst. Man, Cybern. Part C Appl. Rev.
772          IEEE Trans. 41 (2011) 869–884.

773   [67]   M. Green, J.B. Moore, in:, Am. Control Conf. 1985, 1985, pp. 412–417.

774   [68]   Y. Zhu, in:, Multivariable Syst. Identif. Process Control, First, Elsevier Science Ltd,
775          Oxford, 2001, pp. 41–52.

776

777